previous study [15], which includes the refined united atom force field with AMBER99 force field [19] and single point charge (SPC) model [34]. The partial charges of a DPPC molecule were obtained from the study by Chiu et al. [35]. Because we are interested in the dynamical process of a structural change in a bilayer resulting from shock wave irradiation, it may be better to remove the constraints of molecular bond lengths, angles, and dihedrals. Therefore, all bonded interactions in DPPC molecules were calculated in the shock wave simulation. The particle mesh ewald method [36] was used to treat the long-range electrostatic interactions. Both the real-space Ewald and the van der Waals nonbonded interactions were cut off at 1.0 nm. The AMBER 8 set of programs [37] was used for computations.

2.2. Shock wave impulse simulation

As demonstrated in the previous study [15], we modeled a shock wave by its impulse I defined as the time integral of pressure over the shock-pulse duration [7]. From the definition of the impulse, the shock impulse I can be regarded as an increment in the momentum of water divided by an area A on which the shock pressure is exerted. The momentum increment is numerically implemented by the addition of the average velocity V to the thermal velocity of water molecules in a slab adjacent to a bilayer. V is given by

$$V = \frac{I \times A}{mN_{\mathrm{W}}}, \tag{1}$$

where m is the weight of a water molecule and N_{W} is the number of water molecules in the water slab.

Because the choice of a water slab is arbitrary, we consider the water slab of $A \times L_z$, where $A = 42.2\ \mathrm{nm}^2$ was the area of the xy plane of the bilayer system and $L_z = 4.0$ nm was the thickness of the water slab. We set $I = 40$ mPa·s and the number of water molecules in the water slab $N_{\mathrm{W}} = 5423$; the applied average velocity V was 10,394 m/s. Note that V corresponds neither to the sound speed in liquid water nor to the propagation speed of the shock wave. It just represents the increase in the momentum of water molecules due to the shock wave.

In the present study, we slightly modified the shock wave model described above to take account of the incident shock angle. More precisely, the shock wave impulse was divided into the normal (in the z direction) and tangential (in the x direction) components to the bilayer plane (see Fig. 1). That is,

$$I_z = I\cos\theta \quad \text{and} \quad I_x = I\sin\theta, \tag{2}$$

where I_z is the normal component; I_x, the tangential component; and θ, the incident shock angle. V was decomposed to the normal component $V_z = V\cos\theta$ and the tangential component $V_x = V\sin\theta$.

For understanding high-speed and unsteady phenomenon induced by a shock wave impulse in MD, position and velocity scaling of molecules should not be implemented. Therefore, we performed constant *NVE* MD simulation without using the temperature and pressure controls and bond constraints from the initial configuration. The constant energy in this MD is the sum of the total energy in the equilibrium state and the kinetic energy increase induced by adding velocity. Periodic boundary conditions were applied in the three directions. The time step used for the integration of equations of motion was 0.2 fs in order to avoid the excess approach of molecules with large velocities. Owing to the periodic boundary conditions, the simulations were terminated at the time when the effect of the shock impulse reached the boundary at the opposite side of the simulation box in the *z* direction. This is the reason why we prepared a thick water layer. The numerical results shown in the following are the sample averages of 10 production runs for a given θ. From the results of the previous study and preliminary calculations, the system size and the simulation time in the present study were determined in order to focus on the analysis of the essential part of the structural changes in unsteady states.

2.3. Analysis

The changes of hydrophobic chains in the unsteady states can be explained in terms of an averaged instantaneous chain order parameter $\hat{S}_{CD}$ [15],

$$\hat{S}_{CD} = -\frac{1}{2}\left(\frac{1}{N_C}\sum_{i=1}^{N_C}\frac{1}{2}\left(3\cos^2\Theta_i - 1\right)\right), \tag{3}$$

where Θ_i is the angle between the axis of the *i*th molecular axis and the bilayer normal (the *z* axis) and N_C (= 28) is the number of carbons in both *sn*-1 and *sn*-2 chains. Θ_i is evaluated from the instantaneous configurations of lipid molecules. Note that Θ_i in the upper layer is calculated with respect to the bilayer director as pointed out in Ref. [31], because the lipid molecules in the upper layer tilt (see the Results section).

The lateral movement of lipid molecules is characterized by the averaged lateral

displacement of the mass center positions of the headgroups of lipid molecules $L(t)$ defined by

$$L(t) = \frac{1}{N_L} \sum_{i=1}^{N_L} \left| x_i(t) - x_i(0) \right|, \tag{4}$$

where x_i is the x coordinate of the mass center position of the headgroup of the ith molecule, and $N_L (= 64)$ is the number of DPPC molecules in the upper or lower layer.

3. Results

3.1. Collapse and rebound of bilayers

The most outstanding change in a bilayer by the action of a shock wave is the change in the bilayer thickness, which is defined as the distance between the phosphorus atoms of lipid molecules in the upper and lower layers [15]. Figure 2 shows the temporal changes of the bilayer thickness caused by the shock wave impulses of 40 mPa•s for $\theta = 0°$, $30°$, and $60°$. The bilayer thickness became minimum at 530, 590, and 810 fs for $\theta = 0°$, $30°$, and $60°$, respectively. The normalized time t^* in Fig. 2 is defined such that the minimum of bilayer thickness occurs at $t^* = 1$. That is, the bilayer thickness is decreasing during $0 < t^* < 1$ (i.e., collapse stage); then, the bilayer thickness starts to increase after $t^* = 1$ (i.e., rebound stage) regardless of the incident shock angle conditions. In the following the normalized time $t^* = 1$ corresponds to 530, 590, and 810 fs in real time for $\theta = 0°$, $30°$, and $60°$, respectively.

In each incident angle condition, the duration of the rebound stage ($1 < t^*$) is longer than that of the collapse stage ($0 < t^* < 1$). The rebound stage was not completed within the present simulation because of the periodic boundary conditions (see the Methods section). However, the essential points can be clarified as demonstrated below.

The change in the bilayer thickness is expected to be due to the postural changes of lipid molecules. In Fig. 3, we show a series of snapshots of postural changes of typical lipid molecules in the upper and lower layers induced by the shock wave with $\theta = 60°$. By the action of the shock wave, the hydrophobic chains bend (Figs. 3(a)-(c)) and then slightly recover (Figs. 3(d) and 3(e)). Figure 4 shows temporal changes of $\hat{S}_{CD}$ for $\theta = 60°$, normalized by those in the initial state (ca. −0.16). The order parameters obviously

decrease in the collapse stage and gradually recover in the rebound stage. On comparison with the result in Fig. 2, it is confirmed that the decrease in the bilayer thickness was due to this chain disorder. This result is consistent with the previous simulation result [15].

3.2 Lateral movement of lipid molecules

The oblique incidence of a shock wave yields unsteady shear on the bilayer surface. In this simulation, the shear is induced by the tangential momentum change of water molecules adjacent to the bilayer surface (see the Methods section). In Fig. 3, the effect of shear appears as the lateral movement of the lipid molecules in the upper layer. Figure 5 shows the time evolution of the averaged lateral displacements in the upper and lower layers. As pointed out in the previous study [15], the simple shock wave interaction ($\theta = 0^\circ$) enhances the lateral displacement. However, the displacement in the upper layer significantly increases with the incident shock angle from 0° to 60°. In fact, the displacement induced by the shock wave with $\theta = 60^\circ$ becomes 1.5 nm at $t^* = 2$, which is ten times larger than that with $\theta = 0^\circ$. Here, we remark that the lateral displacements of lipid molecules for $\theta = 30^\circ$ and 60° continue to increase even in the rebound stage. On the other hand, the lateral displacement in the lower layer is one order of magnitude smaller than that in the upper layer (Fig. 5 inset).

3.3. Tilt of lipid molecules

From the snapshots in Fig. 3, it is clear that the lipid molecule in the upper layer tilts by the action of incident shock wave. Here, we define the tilt angle as follows: (i) atom positions of a lipid molecule are projected onto the *xz* plane; (ii) a straight line is fitted to these projected positions; (iii) the tilt angle θ_t is obtained from the angle formed between this straight line and the *z* axis (see Fig. 3(e)). The tilt angle in the initial state ($t^* = 0$) calculated here has a wide distribution centered around zero degree, which would be tantamount to that in the equilibrium state of another study [24] although they used a different force field and their tilt angle is defined as that between a vector formed by alternating carbon units along the lipid tails and the bilayer normal axis.

Figure 6(a) shows the tilt angle distributions of the lipid molecules in the upper layer at $t^* = 2$. In the case of $\theta = 0^\circ$, the distribution of tilt angles is hardly changed from that in

the initial state. On the contrary, the distributions for $\theta = 30^\circ$ and 60° shift to the positive side. In Fig. 6(b), we show the temporal changes of the tilt angles averaged for all lipid molecules in the upper layer. Obviously, the averaged tilt angles for $\theta = 30^\circ$ and 60° increase with time and reach maximum values at around $t^* = 2$ (21°, and 32°, respectively). The maximum values are in agreement with those in Ref. [31] on the interaction of steady shear flows with lipid bilayers. In the present unsteady simulation, the lipid alignment is completed within $t^* = 2$. Thus, the simulation limited to $0 < t^* < 2.0$ is adequate to analyze the essential part of the structural changes in unsteady states. Interestingly, whereas the lateral movement of lipid molecules persists as shown in Fig. 5, their tilts are saturated (Fig. 6(b)). However, this will not be discussed in this paper.

The tilt angles averaged in the lower layer did not change (data not shown). We emphasize that this is not due to the restriction of simulation time because the steady simulation of shear flow also obtained the same result [31].

3.4. Water penetration into the hydrophobic region

In the equilibrium state water molecules hardly exist in the hydrophobic region [18] and the event of water penetration into the hydrophobic region rarely occurs in the time scale of MD simulations [38, 39]. On the other hand, under the action of shock waves the water penetration into the hydrophobic region was observed in the time scale of picoseconds (See Fig.3), which is important for subsequent water pore formation in a bilayer [40] and cell membrane permeabilization [4, 6, 9, 15]. Figure 7 shows the temporal changes of the number of water molecules delivered into the hydrophobic region for $\theta = 0^\circ$, 30°, and 60°. Here, the hydrophobic region is defined as the region between the carbonyl groups in *sn*-1 chains in the upper and lower layers [15]. Most of the water molecules penetrated are from the upper water layer. The water penetration in the intermediate stage of the collapse stage ($0.25 < t^* < 0.75$) is smaller in the larger incident angle condition. By contrast, in the intermediate stage of the rebound stage ($1.25 < t^* < 1.75$), the water penetration is larger in the larger incident angle condition. As a result, the total number of delivered water molecules amounts to almost 100 for all cases of $\theta = 0^\circ$, 30°, and 60°, indicating the fact that the water penetration in $0 < t^* < 2.0$ is insensitive to the incident angles, at least for

the case of $I = 40$ mPa·s.

The trend in the collapse stage is clearly a direct consequence of the difference in the impulse intensity in the normal direction. In the rebound stage, on the other hand, a large amount of the normal component of the momentum has been transferred through the upper layer, as shown in the next subsection; instead, the lateral displacements and tilts of lipid molecules in the upper layer are prominent as demonstrated in Figs. 5, and 6. Therefore, the penetration of water molecules near the upper layer in the rebound stage may be governed by these lipid structural changes [23, 25, 41].

3.5 Momentum transfer across bilayers

It is interesting to assess the amount of momentum transferred across the bilayer by the shock wave because the momentum transfer is related to the transfer characteristics of the bilayer or a subsequent flow induction. The momentum transfer can be estimated from the changes of momentum in the lower water layer. In Fig. 8, we show temporal changes of the normal and tangential components of momentum for $\theta = 60^\circ$ normalized by the corresponding values initially added to the water slab. Both the components begin to increase at around $t^* = 1.0$, and in particular, the normal component attains 60% of its initial value at $t^* = 2.0$, while the increase in the tangential component remains very small. That is, only the normal component of the added oblique momentum is substantially transferred across the bilayer within the time scale of the order of picoseconds. This certainly affects the flow induction in the cytoplasm and this will be discussed in detail in the final section. Note that the rest of the normal component, 40% of its initial value, still stays inside the bilayer at $t^* = 2.0$ as can be seen from Fig. 3(e), where the downward movement of lipid molecules persists.

The ratio between the sliding force per unit of bilayer area and the velocity difference between the two leaflets of a bilayer is called the intermonolayer friction coefficient b, which is one of the measures of the intermonolayer flow behavior [32, 33, 42]. b is given by $b = F / A\Delta V$, where F is the sliding force, A is the bilayer area, and ΔV is the velocity difference. Usually, b is evaluated in lengthy steady simulations, however, it can be obtained in an unsteady simulation as follows: F for $\theta = 60^\circ$ was roughly calculated from the momentum change of the lower layer (17753.06 N·s/mol) divided by the time

interval $0 < t^* < 2.0$ (1.56 ps); the sliding force between the lower monolayer and lower water layer was assumed to be zero because of the very small amount of momentum transferred to the lower water layer (Fig. 8 inset); the slip velocity was the instantaneous velocity difference of the mass centers of the upper and lower layers at $t^* = 2.0$ (571.74 m/s). As a result, we obtained $b = 8 \times 10^5$ Pa m^{-1}s at $t^* = 2.0$ in the unsteady state using the present simulation results. Surprisingly, the intermonolayer friction coefficient in the present study is almost the same as that obtained in the coarse-grained MD simulations in Refs. [32, 33] (typically 1×10^6 Pa m^{-1}s) by applying Lees-Edwards boundary conditions, although the normal component of momentum was not considered in these simulations.

4. Summary and discussion

This study aimed at investigating the effect of incident shock angles on the structural changes of a lipid bilayer by using unsteady nonequilibrium MD simulations. The simulation results revealed that the half of the bilayer directly exposed to shock waves is sensitive to an incident shock wave; therefore, the lateral displacement and the tilts of lipid molecules are enhanced with an increase in the incident shock angle from 0° to 60° within the time scale of the order of picoseconds (Fig. 9(a)). On the other hand, the other half of the bilayer is found to be insensitive to the change of the incident shock angle. This difference in sensitivity to the incident shock wave results in the fact that only the normal component of the applied oblique impulse is transferred across the bilayer.

Finally, we discuss the possible streaming of the cytoplasm induced by shock waves. As shown in Fig. 8, the normal component of the applied momentum promptly transfers across the bilayer, whereas the tangential component hardly transfers. Here, let us assume a cell to be a sphere and a shock wave impulse is applied downward on the surface of the sphere (Fig. 9(b) left). The intensity of the applied momentum along membrane normal is largest on the top of the sphere, and it is reduced to zero along the meridian of the sphere. Accordingly, the momentum distribution has a maximum (Fig. 9(b) right), which will result in the formation of a jet-like streaming in the cytoplasm. In reality, the cell membrane is usually undulating; hence, several momentum maxima with different directions may be produced beneath the membrane. Therefore, the streaming in the cytoplasm caused by the shock wave will be comprised of several jet-like flows emerged

from several momentum maxima, and the entire flow pattern in the cytoplasm will become complex. The mixing or homogenization of plasmid [10] and fluorescein [7] throughout the cell cytoplasm appears to be enhanced by jet-like flows.

Acknowledgments

TK acknowledges (i) the Encouraging Development of Strategic Research Center, Special Coordination Funds for Promoting Science and Technology, MEXT, Japan, (ii) Grant-in-Aid for Scientific Research (B) (17300168), (iii) Grant-in-Aid for Exploratory Research (18650140), (iv) Research on Advanced Medical Technology, The Ministry of Health Labor and Welfare (H19-nano-010).

References

[1] S. Gambihler, M. Delius, Transient increase in membrane permeability of L1210 cells upon exposure to lithotripter shock waves in vitro, Naturwissenschaften 79 (1992) 328-329.

[2] S. Gambihler, M. Delius, J.W. Ellwart, Permeabilization of the plasma membrane of L1210 mouse leukemia cells using lithotripter shock waves, J. Membr. Biol. 141 (1994) 267-275.

[3] U. Lauer, E. Burgelt, Z. Squire, K. Messmer, P.H. Hofschneider, M. Gregor, M. Delius, Shock wave permeabilization as a new gene transfer method, Gene Ther. 4 (1997) 710-715.

[4] L.B. Feril, T. Kondo, S. Umemura, K. Tachibana, H.A. Manalo, P. Riesz, Sound Wave and Antineoplastic Drugs:The Possibility of an Enhanced Combined Anticaner Therapy, J. Med. Ultrasonics 29 (2002) 173-187.

[5] S. Mehier-Humbert, R.H. Guy, Physical methods for gene transfer: Improving the kinetics of gene delivery into cells, Adv. Drug Delivery Rev. 57 (2005) 733-753.

[6] M. Kambe, N. Ioritani, R. Kanamaru, Enhancement of chemotherapeutic effects with focused shock waves: extracorporeal shock wave chemotherapy (ESWC), Hum. Cell 10 (1997) 87-94.

[7] T. Kodama, M.R. Hamblin, A.G. Doukas, Cytoplasmic molecular delivery with shock waves: importance of impulse, Biophys. J. 79 (2000) 1821-1832.

[8] J. Sundaram, B.R. Mellein, S. Mitragotri, An experimental and theoretical analysis of ultrasound-induced permeabilization of cell membranes, Biophys. J. 84 (2003) 3087-3101.

[9] S. Mehier-Humbert, T. Bettinger, F. Yan, R.H. Guy, Plasma membrane poration induced by ultrasound exposure: Implication for drug delivery, J. Contr. Rel. 104 (2005) 213-222.

[10] S. Mehier-Humbert, T. Bettinger, F. Yan, R.H. Guy, Ultrasound-mediated gene delivery: Kinetics of plasmid internalization and gene expression, J. Contr. Rel. 104 (2005) 203-211.

[11] T. Kodama, Y. Tomita, K.I. Koshiyama, M.J.K. Blomley, Transfection effect of

microbubbles on cells in superposed ultrasound waves and behavior of cavitation bubble, Ultrasound in Med. Biol. 32 (2006) 905-914.
[12] W.D. O'Brien, Jr., Ultrasound-biophysics mechanisms, Prog. Biophys. Mol. Biol. 93 (2007) 212-255.
[13] D.L. Miller, Overview of experimental studies of biological effects of medical ultrasound caused by gas body activation and inertial cavitation, Prog. Biophys. Mol. Biol. 93 (2007) 314-330.
[14] E. VanBavel, Effects of shear stress on endothelial cells: Possible relevance for ultrasound applications, Prog. Biophys. Mol. Biol. 93 (2007) 374-383.
[15] K. Koshiyama, T. Kodama, T. Yano, S. Fujikawa, Structural Change in Lipid Bilayer and Water Penetration Induced by Shock Wave: Molecular Dynamics Simulations, Biophys. J. 91 (2006) 2198-2205.
[16] U. Seifert, Configurations of fluid membranes and vesicles, Adv. Phys. 46 (1997) 13-137.
[17] M. Lokhandwalla, B. Sturtevant, Mechanical haemolysis in shock wave lithotripsy (SWL): I. Analysis of cell deformation due to SWL flow-fields, Phys. Med. Biol. 46 (2001) 413-437.
[18] D.P. Tieleman, S.J. Marrink, H.J.C. Berendsen, A computer perspective of membranes: molecular dynamics studies of lipid bilayer systems, Biochim. Biophys. Acta-Rev. Biomemb. 1331 (1997) 235-270.
[19] A.M. Smondyrev, M.L. Berkowitz, United atom force field for phospholipid membranes: Constant pressure molecular dynamics simulation of dipalmitoylphosphatidicholine/water system, J. Comp. Chem. 20 (1999) 531-545.
[20] C. Anezo, A.H. de Vries, H.D. Holtje, D.P. Tieleman, S.J. Marrink, Methodological issues in lipid bilayer simulations, J. Phys. Chem. B 107 (2003) 9424-9433.
[21] M. Patra, M. Karttunen, M.T. Hyvonen, E. Falck, P. Lindqvist, I. Vattulainen, Molecular dynamics simulations of lipid bilayers: Major artifacts due to truncating electrostatic interactions, Biophys. J. 84 (2003) 3636-3645.
[22] W.L. Ash, M.R. Zlomislic, E.O. Oloo, D.P. Tieleman, Computer simulations of membrane proteins, Biochim. Biophys. Acta-Rev. Biomemb. 1666 (2004) 158-189.
[23] M. Kupiainen, E. Falck, S. Ollila, P. Niemela, A.A. Gurtovenko, M.T. Hyvonen, M. Patra, M. Karttunen, I. Vattulainen, Free volume properties of sphingomyelin, DMPC, DPPC, and PLPC bilayers, J.Comp. Theor. Nanoscience 2 (2005) 401-413.
[24] S. Leekumjorn, A.K. Sum, Molecular studies of the gel to liquid-crystalline phase transition for fully hydrated DPPC and DPPE bilayers, Biochim. Biophys. Acta-Biomemb. 1768 (2007) 354-365.
[25] K. Murzyn, W. Zhao, M. Karttunen, M. Kurdziel, T. Rog, Dynamics of water at membrane surfaces: Effect of headgroup structure, Biointerphases 1 (2006) 98-105.
[26] J.G. Jeon, G.A. Voth, The dynamic stress responses to area change in planar lipid bilayer membranes, Biophys. J. 88 (2005) 1104-1119.
[27] H. Leontiadou, A.E. Mark, S.J. Marrink, Molecular dynamics simulations of hydrophilic pores in lipid bilayers, Biophys. J. 86 (2004) 2156-2164.
[28] D.P. Tieleman, The molecular basis of electroporation, BMC Biochem. 5 (2004) 1-10.
[29] Q. Hu, S. Viswanadham, R.P. Joshi, K.H. Schoenbach, S.J. Beebe, P.F. Blackmore, Simulations of transient membrane behavior in cells subjected to a high-intensity ultrashort electric pulse, Phys. Rev. E 71 (2005) 0319141-0319149.
[30] M. Tarek, Membrane electroporation: A molecular dynamics simulation, Biophys. J. 88 (2005) 4045-4053.
[31] P.D. Blood, G.S. Ayton, G.A. Voth, Probing the molecular-scale lipid bilayer

response to shear flow using nonequilibrium molecular dynamics, J. Phys. Chem. B 109 (2005) 18673-18679.
[32] S.A. Shkulipa, W.K. den Otter, W.J. Briels, Surface viscosity, diffusion, and intermonolayer friction: Simulating sheared amphiphilic bilayers, Biophys. J. 89 (2005) 823-829.
[33] W.K. den Otter, S.A. Shkulipa, Intermonolayer friction and surface shear viscosity of lipid bilayer membranes, Biophys. J. 93 (2007) 423-433.
[34] H.J.C. Berendsen, J.P.M. Postma, W.F. Gunsteren, J.H., Interaction models for water in relation to protein hydration, in: B. Pullman (Ed.), Intermolecular Forces, D. Reidel Publishing Company, 1981, pp. 331-342.
[35] S.W. Chiu, M. Clark, V. Balaji, S. Subramaniam, H.L. Scott, E. Jakobsson, Incorporation of Surface-Tension into Molecular-Dynamics Simulation of an Interface - a Fluid-Phase Lipid Bilayer-Membrane, Biophys. J. 69 (1995) 1230-1245.
[36] U. Essmann, L. Perera, M.L. Berkowitz, T. Darden, H. Lee, L.G. Pedersen, A Smooth Particle Mesh Ewald Method, J. Chem. Phys. 103 (1995) 8577-8593.
[37] D.A. Pearlman, D.A. Case, J.W. Caldwell, W.S. Ross, T.E. Cheatham, S. Debolt, D. Ferguson, G. Seibel, P. Kollman, Amber, a Package of Computer-Programs for Applying Molecular Mechanics, Normal-Mode Analysis, Molecular-Dynamics and Free-Energy Calculations to Simulate the Structural and Energetic Properties of Molecules, Comp. Phys. Comm. 91 (1995) 1-41.
[38] S.J. Marrink, H.J.C. Berendsen, Simulation of Water Transport through a Lipid-Membrane, J. Phys. Chem. 98 (1994) 4155-4168.
[39] T.X. Xiang, Translational diffusion in lipid bilayers: Dynamic free-volume theory and molecular dynamics simulation, J. Phys. Chem. B 103 (1999) 385-394.
[40] K. Koshiyama, T. Kodama, T. Yano, S. Fujikawa, Molecular dynamics simulation of water pore formation in lipid bilayer induced by shock waves, AIP Conf. Proc. 829 (2006) 583-587.
[41] J. Repakova, P. Capkova, J.M. Holopainen, I. Vattulainen, Distribution, orientation, and dynamics of DPH probes in DPPC bilayer, J. Phys. Chem. B 108 (2004) 13438-13448.
[42] E. Evans, A. Yeung, Hidden Dynamics in Rapid Changes of Bilayer Shape, Chem. Phys. Lipids 73 (1994) 39-56.

Figure Legends

Figure 1.

Schematic diagram of the interaction of a shock wave with a lipid bilayer, where θ is the

incident angle between the bilayer normal and the direction of shock wave propagation.

Figure 2.

Temporal changes of the bilayer thickness in the simulations for $\theta = 0°$, $30°$, and $60°$. The bilayer thickness is normalized by that in the initial state (ca. 4.0 nm). Note that in the following figures the normalized time $t^* = 1$ corresponds to 530, 590, and 810 fs in real time for $\theta = 0°$, $30°$, and $60°$, respectively.

Figure 3.

Snapshots of postural changes of typical lipid molecules in upper and lower layers induced by the shock wave with $\theta = 60°$. The yellow bars represent the headgroup of a lipid molecule; the orange bars, the hydrophobic chains; and the red spheres, water molecules. The yellow arrow in the snapshot of $t^* = 0$ denotes the propagation direction of the incident shock wave. The other lipid molecules are eliminated for clarity.

Figure 4.

Temporal changes of averaged instantaneous order parameter for $\theta = 60°$. The order parameters are normalized by those in the initial state.

Figure 5.

Lateral displacement of the mass center of lipid head groups for $\theta = 0°$, $30°$, and $60°$ in the upper layer and that in the lower layer (inset).

Figure 6.

(a) Tilt angle distributions of the lipid molecules in the upper layer for $\theta = 0°$, $30°$, and $60°$ at $t^* = 2.0$. (b) Temporal changes of the averaged tilt angle of lipid molecules in the upper layer. Note that the average equilibrium angle in the initial stage is taken as $0°$ in Fig. 6(b).

Figure 7.

Number of the water molecules delivered into the hydrophobic region of a bilayer induced by shock wave with $\theta = 0°$, $30°$, and $60°$.

Figure 8.

Temporal changes of the momentum of the lower water layer in the z direction (normal component) and that in the x direction (tangential component, inset) for $\theta = 60°$.

Figure 9.

Schematic diagram of (a) structural changes of cell membranes and (b) expected momentum transfer across the membrane in a cell by shock waves.

Figure 1

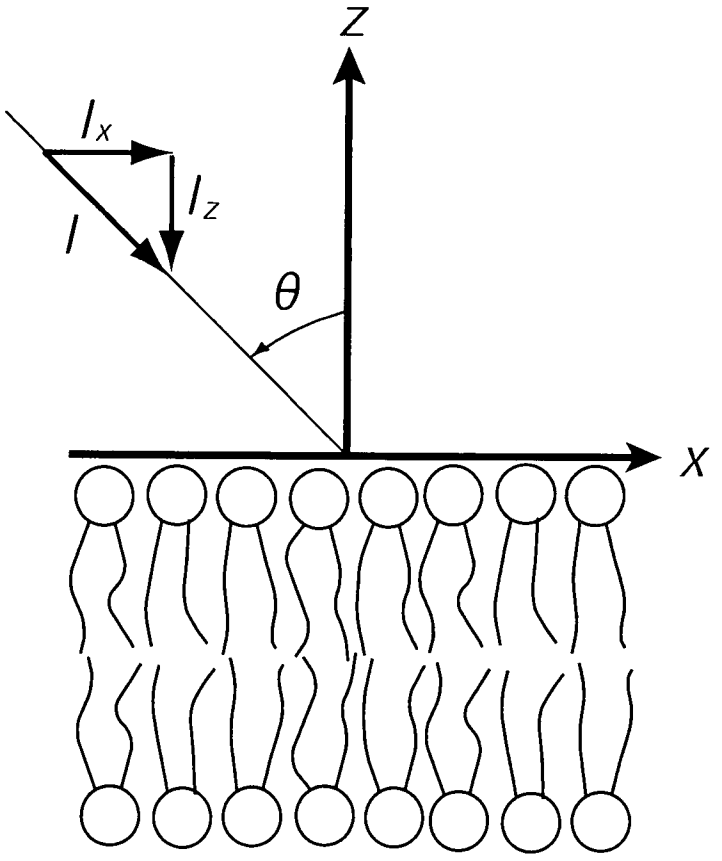

Figure 2

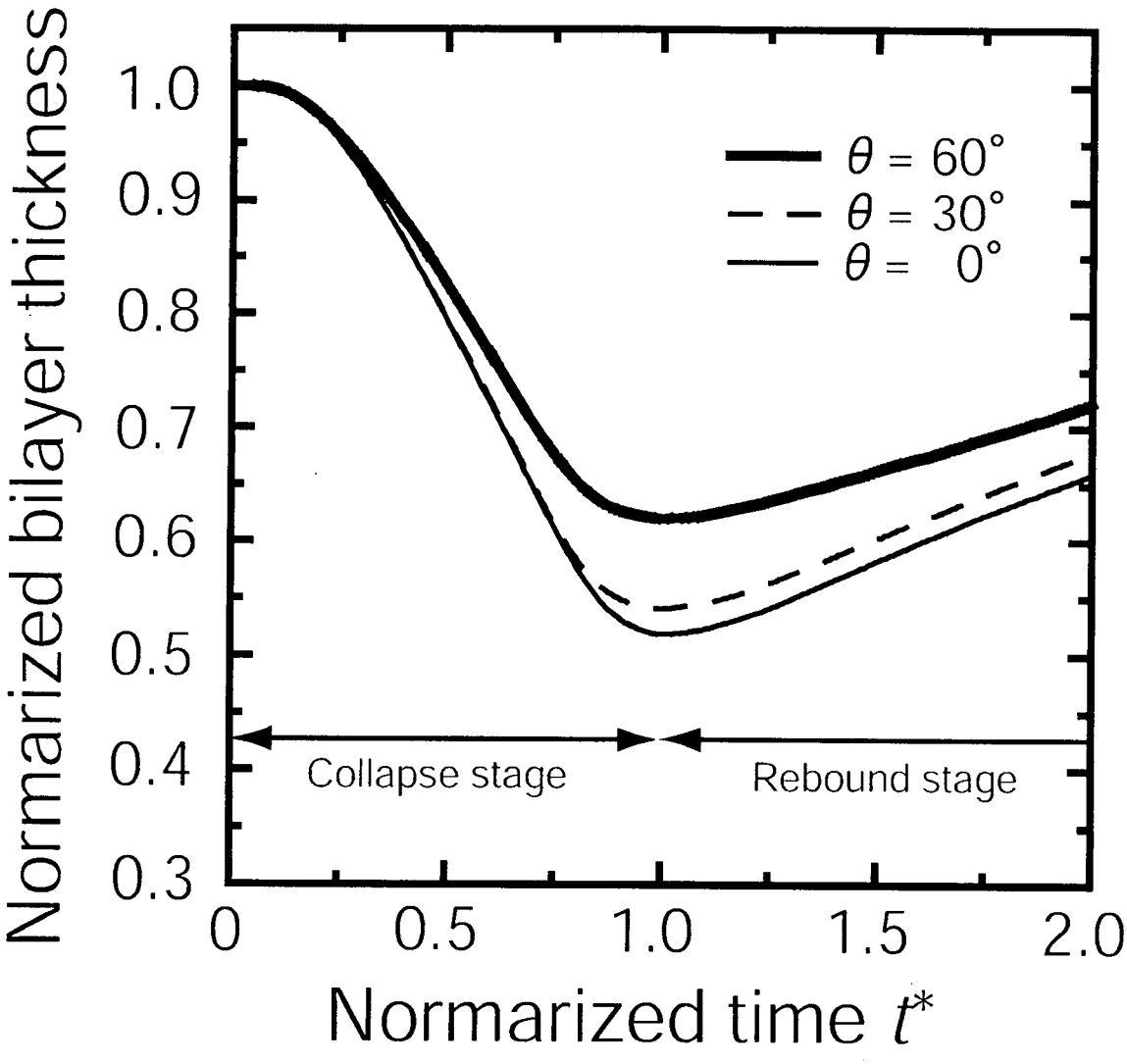
Normarized bilayer thickness
1.0
0.9
0.8
0.7
0.6
0.5
0.4
0.3
θ = 60°
θ = 30°
θ = 0°
Collapse stage
Rebound stage
0
0.5
1.0
1.5
2.0
Normarized time t*

Figure 3
Click here to download high resolution image

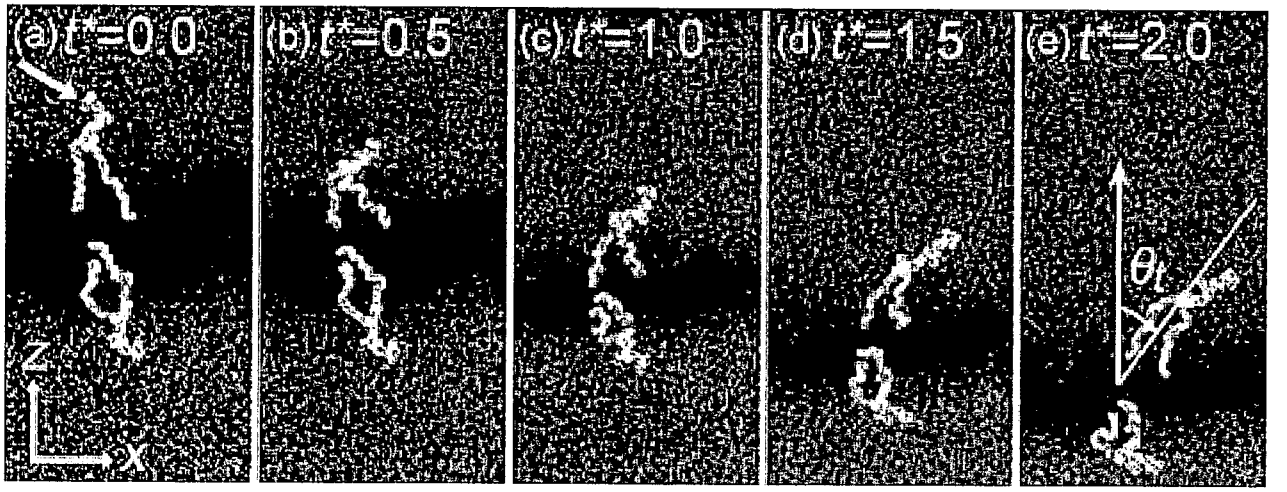

Figure 4

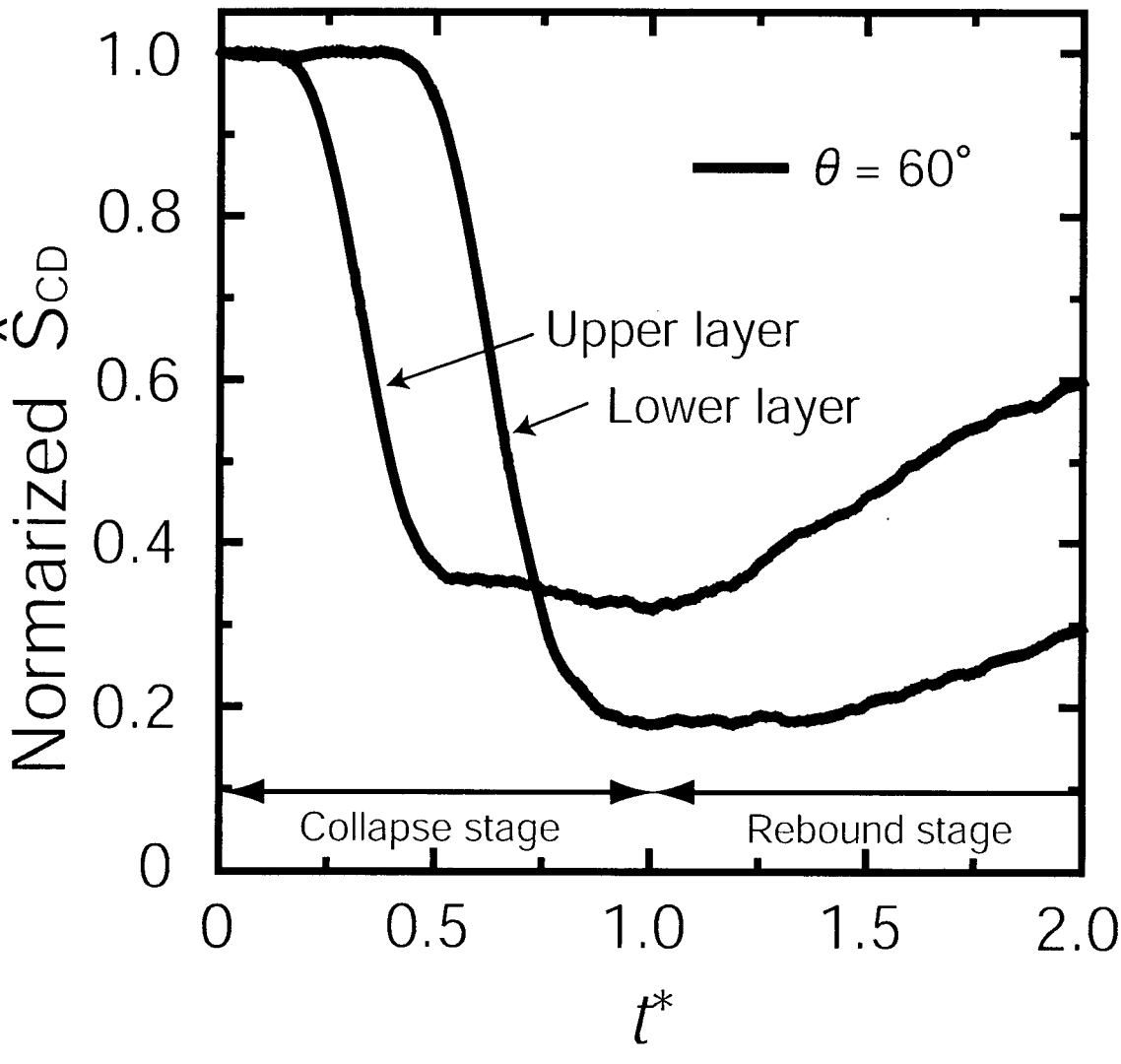
1.0
0.8
0.6
0.4
0.2
0
Normarized $\hat{S}_{CD}$
θ = 60°
Upper layer
Lower layer
Collapse stage
Rebound stage
0
0.5
1.0
1.5
2.0
t^*

Figure 5

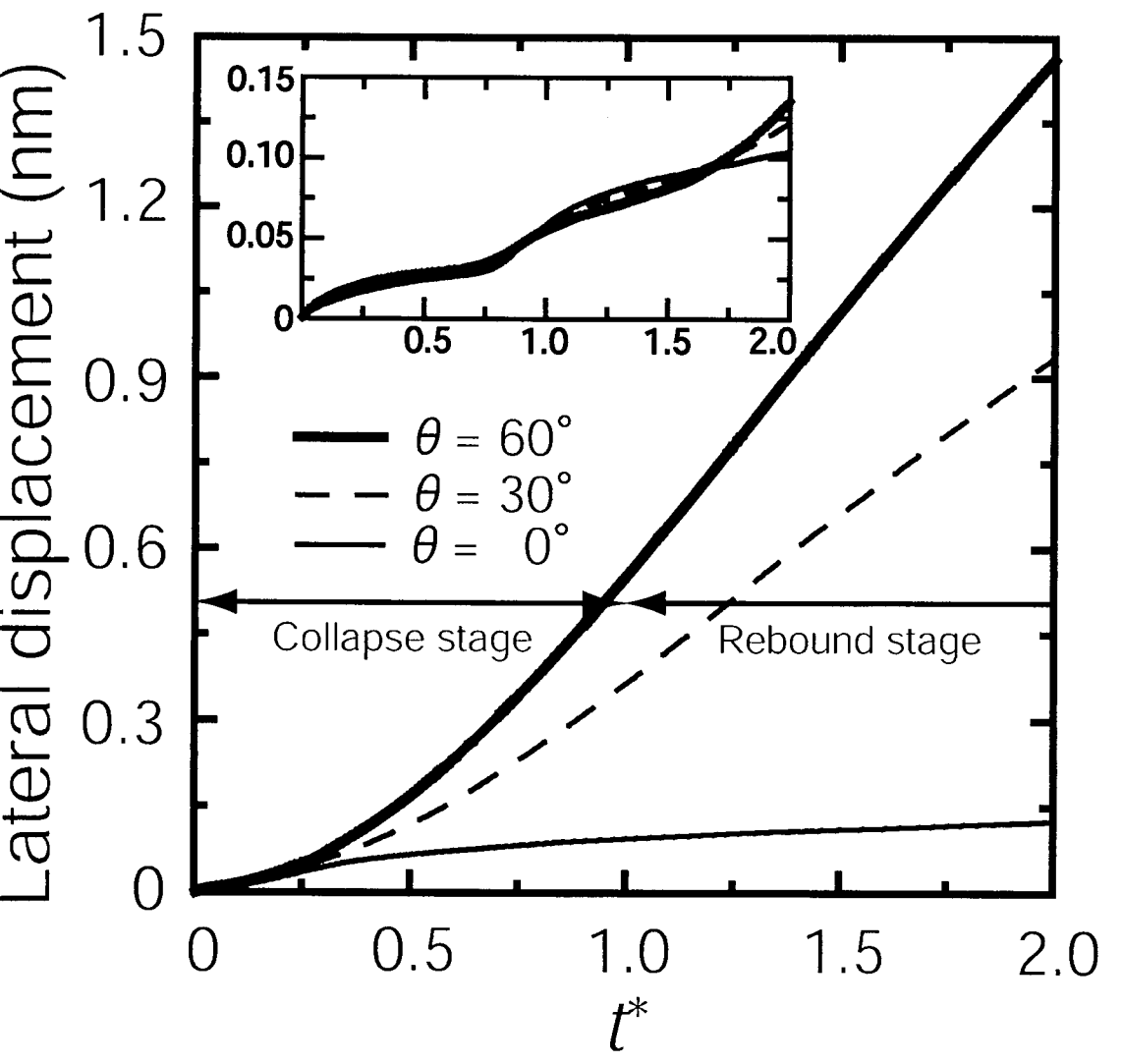
Lateral displacement (nm)
1.5
1.2
0.9
0.6
0.3
0
0.15
0.10
0.05
0
0.5
1.0
1.5
2.0
θ = 60°
θ = 30°
θ = 0°
Collapse stage
Rebound stage
0
0.5
1.0
1.5
2.0
t*

Figure 6

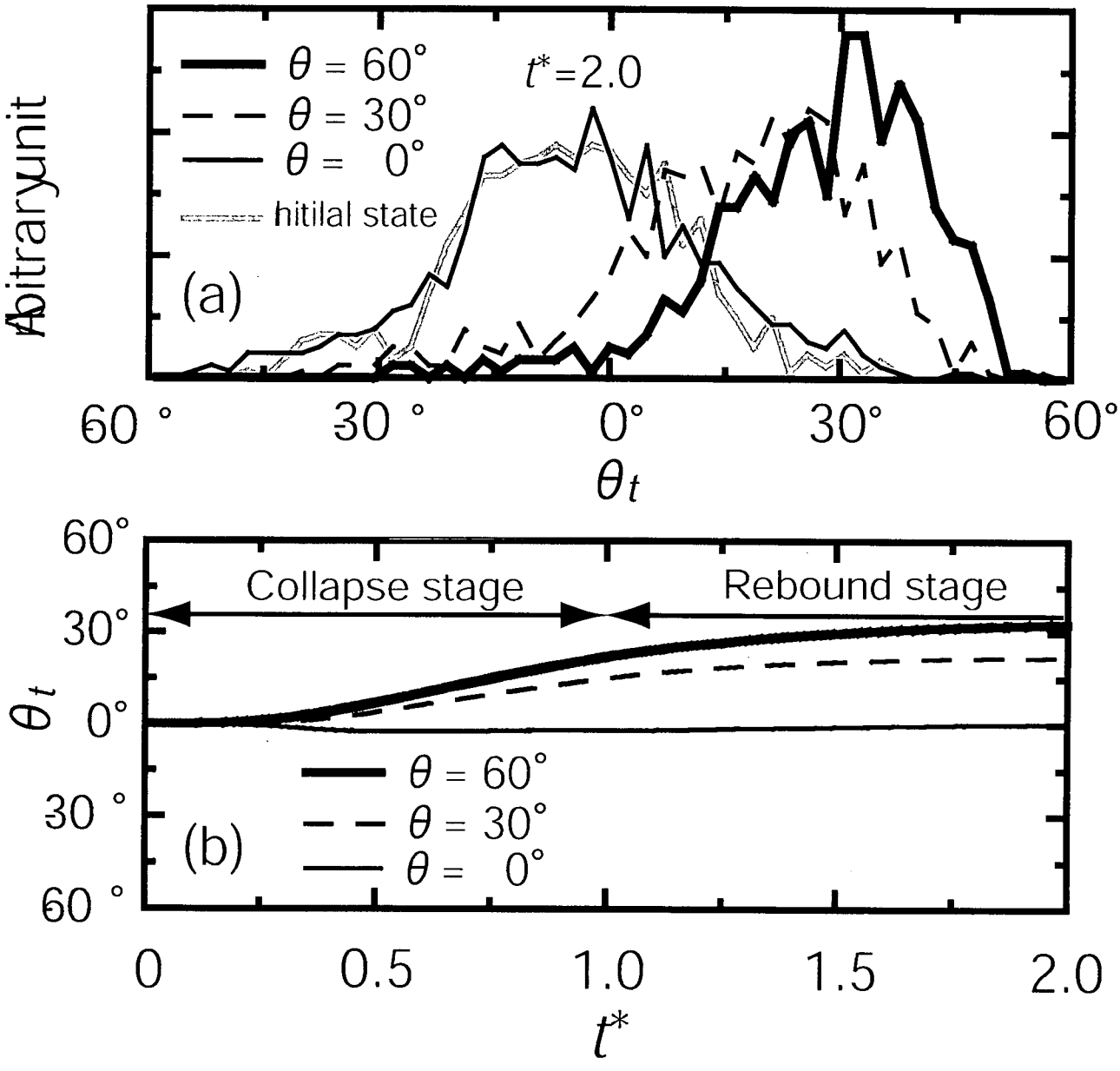
θ = 60°
θ = 30°
θ = 0°
hitilal state
t*=2.0
(a)
Abitraryunit
60 °
30 °
0°
30°
60°
θt
60°
30°
0°
30 °
60 °
Collapse stage
Rebound stage
θt
θ = 60°
θ = 30°
θ = 0°
(b)
0
0.5
1.0
1.5
2.0
t*

Figure 7

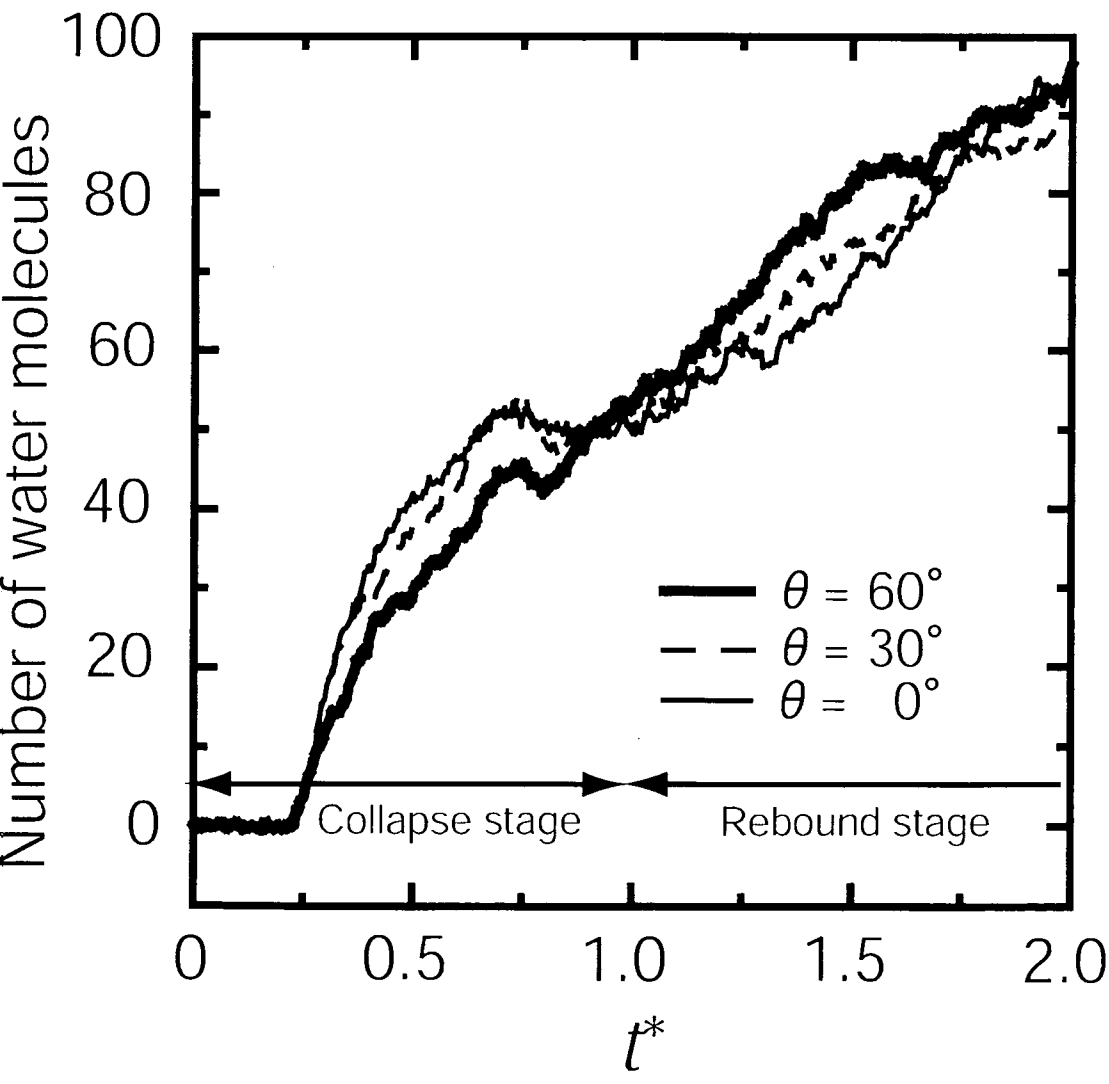
100
80
60
40
20
0
Number of water molecules
0
0.5
1.0
1.5
2.0
t*
θ = 60°
θ = 30°
θ = 0°
Collapse stage
Rebound stage

Figure 8

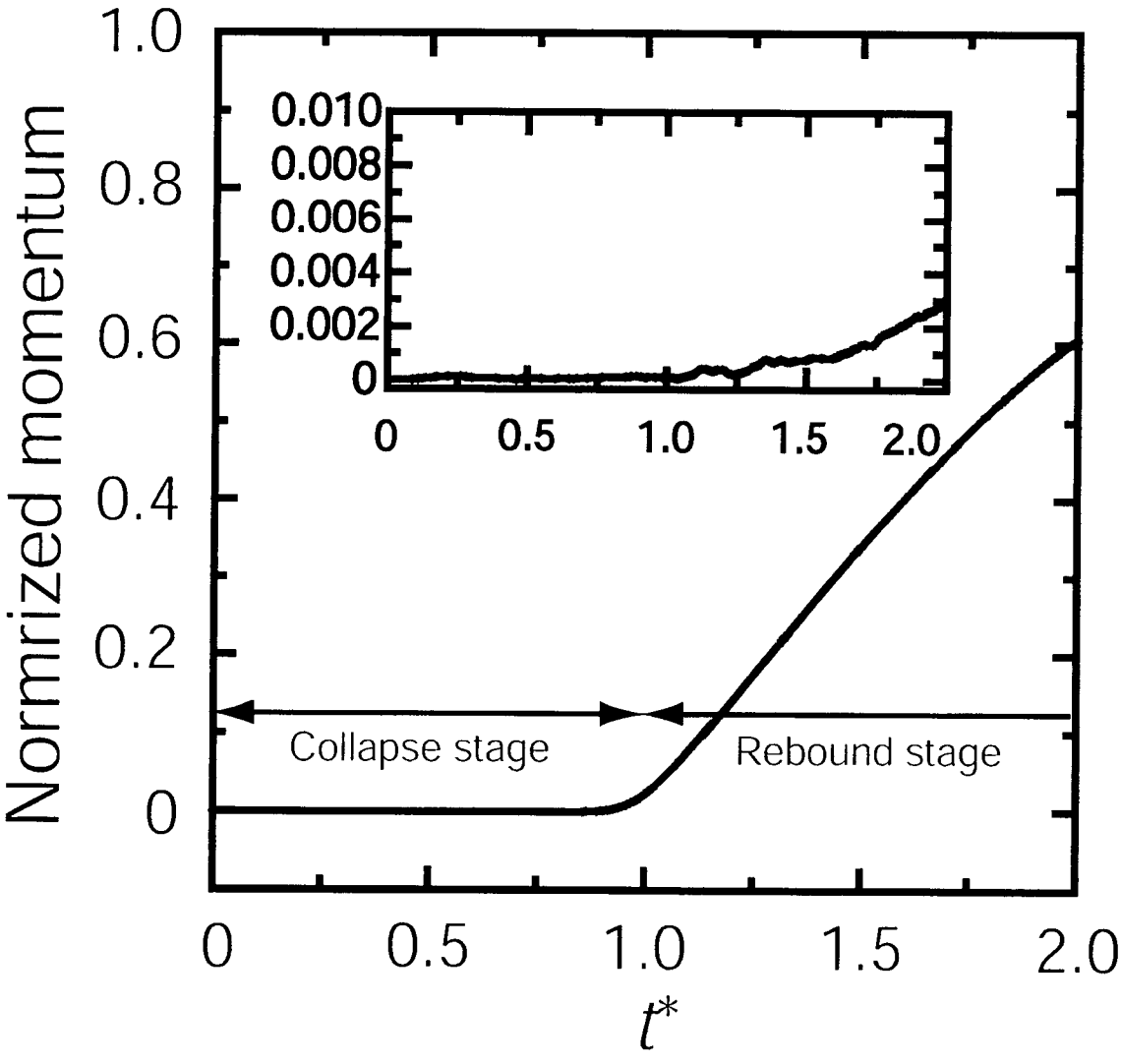
Normrized momentum
1.0
0.8
0.6
0.4
0.2
0
0.010
0.008
0.006
0.004
0.002
0
0
0.5
1.0
1.5
2.0
Collapse stage
Rebound stage
0
0.5
1.0
1.5
2.0
t*